

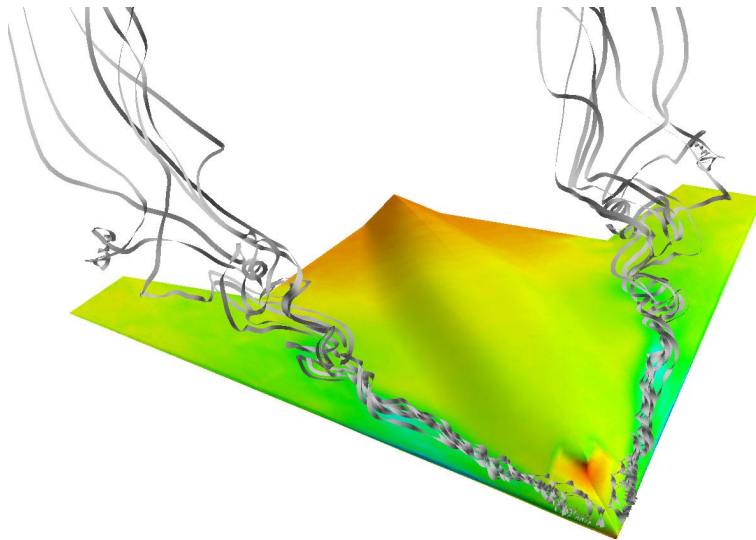


**AIAA 2003-0417**

**Numerical Prediction and Wind Tunnel  
Experiment for a Pitching Unmanned  
Combat Air Vehicle**

Russell M. Cummings, Scott A. Morton,  
Stefan G. Siegel, and Steven Bosscher

The Department of Aeronautics  
United States Air Force Academy  
USAF Academy, CO 80840



**41<sup>st</sup> Aerospace Sciences Meeting**  
6-9 January, 2003  
Reno, Nevada

# Numerical Prediction and Wind Tunnel Experiment for a Pitching Unmanned Combat Air Vehicle

Russell M. Cummings,\* Scott A. Morton,<sup>†</sup> Stefan G. Siegel,<sup>‡</sup> and Steven Bosscher<sup>§</sup>

Department of Aeronautics  
United States Air Force Academy  
USAF Academy, CO 80840

## Abstract

The low-speed flowfield on a generic unmanned combat air vehicle (UCAV) is investigated. A wind tunnel experiment was conducted with the Boeing 1301 UCAV at a variety of angles of attack up to 70 degrees, both static and with various frequencies of pitch oscillation (0.5, 1.0, and 2.0 Hz). In addition, pitching was performed about three longitudinal locations on the configuration, the nose, 35% MAC, and the tail. Solutions to the unsteady, laminar, compressible Navier-Stokes equations were obtained on an unstructured mesh to match results from the static and dynamic experiments. The computational results are compared with experimental results for both static and pitching cases. Details about the flowfield, including vortex formation and interaction, are shown and discussed.

## Nomenclature

$a$	acoustic speed
$\bar{c}$	mean aerodynamic chord, 5.24 in
$C_D$	drag coefficient, $\equiv D / q_\infty S_{ref}$
$C_L$	lift coefficient, $\equiv L / q_\infty S_{ref}$

$f$	pitching frequency, Hz
$k$	reduced frequency, $\equiv \pi f \bar{c} / V_\infty$
$M$	Mach number, $\equiv V / a$
$p$	static pressure, psi
$q$	dynamic pressure, $\equiv \gamma \rho M^2 / 2$
$S_{ref}$	wing planform area, 46.82 in <sup>2</sup>
$t$	physical time, s
$t^*$	non-dimensional time, $\equiv t V_\infty / \bar{c}$
$V$	velocity
$V_\infty$	freestream velocity, 65.4 ft/s
$\alpha$	angle of attack, deg
$\gamma$	ratio of specific heats
$\omega$	rotation rate, $= 2\pi f$
$\infty$	freestream condition

## Introduction

Unmanned combat air vehicles (UCAVs) have shown their value as reconnaissance vehicles, and even tactical weapons, over the past few years. Aircraft such as Predator and Global Hawk are fast becoming essential tools in the day-to-day operations of the military. While the capability of these aircraft will continue to be improved, a need will develop for the vehicles to be able to perform more complex maneuvers, including flying in formation with other UCAV vehicles.

Eventually, UCAVs will be called upon to take advantage of their pilotless state and pull many more g's than manned aircraft. Issues such as control actuation,<sup>1</sup> morphing wings,<sup>2</sup> fuel cell-based propulsion systems,<sup>3</sup> MEMS-based control systems,<sup>4</sup> and semi-autonomous flight<sup>5</sup> will be essential to the further development of these vehicles. One such capability will be utilizing dynamic lift (also known as dynamic stall) due to fast pitch-ups for super-maneuverability and agility.

\* Distinguished Visiting Professor, on leave from the Aerospace Engineering Department, California Polytechnic State University, Associate Fellow AIAA.

<sup>†</sup> Associate Professor, Associate Fellow AIAA.

<sup>‡</sup> Postdoctoral Researcher, Member AIAA.

<sup>§</sup> Visiting Graduate Student, Delft University of Technology.

This paper is declared a work of the U.S. Government and is not subject to copyright protection in the United States.

Dynamic lift utilizes the hysteresis effects of airfoils or wings pitching up at rapid rates to delay the onset of stall. As airfoils pitch up there is a time lag in the separation of flow over the upper surface, which allows for the attainment of higher angles of attack than during static conditions. In addition, leading-edge vortices form that aid in the development of lift. Several researchers have shown the effects of dynamic lift (or dynamic stall) on airfoils, both with experimental and numerical studies.<sup>6-8</sup> In fact, excellent review articles on dynamic stall have been written by Ekaterinaris and Platzer,<sup>9</sup> as well as Carr.<sup>10</sup> Experimental and numerical studies have also been conducted on wings undergoing dynamic stall—see Refs. 11 to 13, for example.

Very little work, however, has been done on studying the dynamic lifting capabilities of full aircraft configurations such as generic UCAVs. This work hopes to better understand the impact of vortex lift and vortex breakdown, coupled with dynamic lift, for these

configurations. The results of the dynamic stall studies for airfoils may be summarized by the lift and pitching moment results shown in Fig. 1. Depending on the pitching frequency, an airfoil will exceed static loads as it pitches up, with lift continuing to increase until separation becomes apparent on the upper surface near the trailing edge (a). Eventually, as the separation region grows, a vortex will form near the leading edge of the airfoil (b). The vortex momentarily increases the rate of lift increase, but eventually the stall region reaches its full extent (c). Finally, as the airfoil pitches down the boundary layer begins reattaching to the upper surface, and finally the flow returns to its original state (d). The combination of flow separation and vortex formation also has a large impact on pitching moment, as can also be seen in Fig. 1. Again, these results are based on two-dimensional airfoils pitching at approximately the same frequencies. It is not known whether these results would be reproduced on a full UCAV configuration.

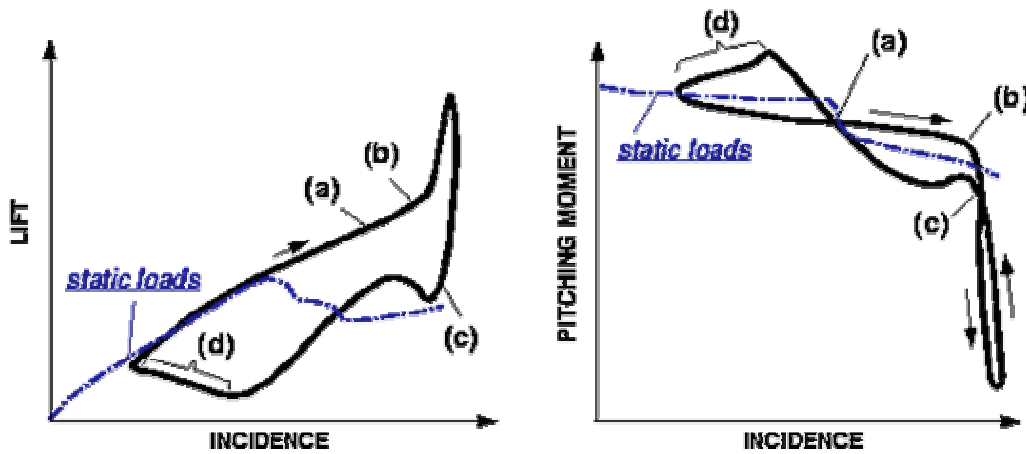
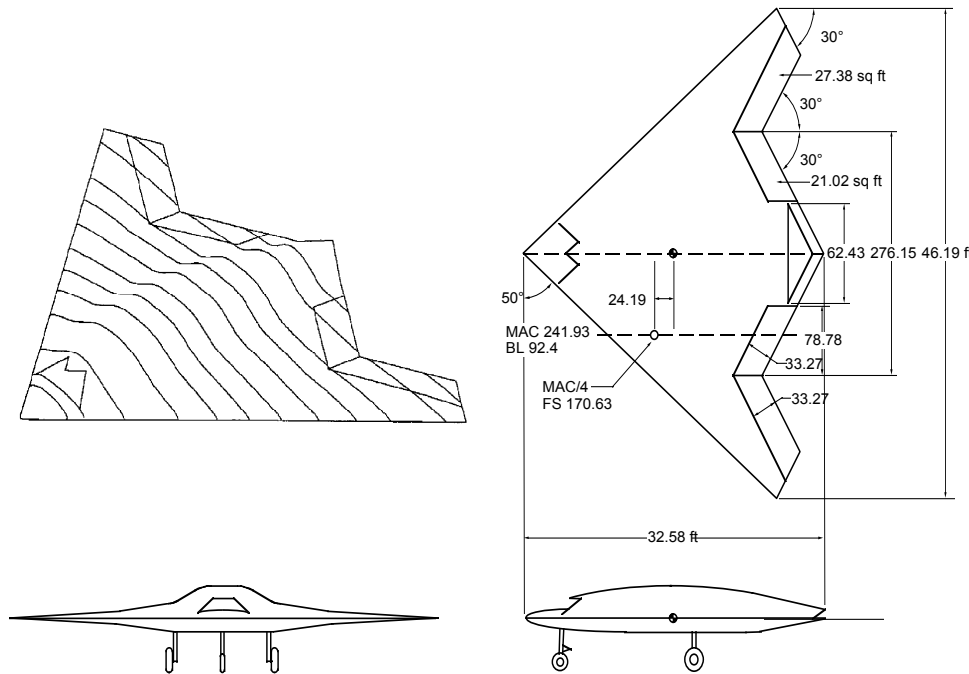


Figure 1. Dynamic Stall Events on an Airfoil (Refs. 9,10, and 14).

### Experimental Results

A full-scale model for the Boeing 1301 UCAV configuration is shown in Fig. 2. The configuration has many similar features to the X-45A UCAV configuration (see Fig. 3). The 1301 configuration has a straight, 50° sweep leading

edge, an aspect ratio of 3.1, a top-mounted engine inlet, and a B-2-like wing planform. The full-scale configuration has a mean aerodynamic chord of 20.2 *ft* and a reference area of 694 *ft*<sup>2</sup>.



**Figure 2. Boeing 1301 UCAV Configuration.**



**Figure 3. X-45A UCAV Configuration (photo from NASA Dryden Flight Research Center).**

A 1:46.2 scale model of the configuration was tested in the USAF Academy 3 ft × 3 ft (0.914 m × 0.914 m) open return low-speed wind tunnel (see Fig. 4). The scaled model has a mean aerodynamic chord of 5.24 in (0.133 m) and a reference area (wing planform area) of 46.82 in<sup>2</sup> (302.1 cm<sup>2</sup>). The tunnel has less than 0.05% freestream turbulence levels at all speeds. The test was conducted at a freestream velocity of 65.4 ft/s (20 m/s), which corresponds to a chord-based Reynolds number of 1.42 × 10<sup>5</sup>. The model was sting-mounted

from the rear, and forces and moments were measured with a six-component force balance, with a normal force range of 50 lb (223 N). Both static and dynamic testing was done; forces during the dynamic runs were obtained by subtracting the force history with the tunnel off from the dynamic data. The balance calibration was accurate to ±0.5% of the full measurement force of the balance, or 0.25 lb (1.12 N). The lift and drag coefficients are only accurate to ±1.9% due to inaccurate readings of the room static pressures on the testing days.

The dynamic pitching was done with a shifted cosine oscillation, starting at a certain angle of attack and pitching up to twice the peak amplitude of the cosine wave, then back to the original angle of attack.

$$\alpha(t) = \alpha_0 + m^\circ (1 - \cos(\omega t))$$

where  $\alpha_0$  and  $m$  were varied to obtain results for  $0^\circ \leq \alpha \leq 45^\circ$  in three pitching cycles. This pitching function was used since it produces a motion without any discontinuities in acceleration or velocity at the beginning and end of the motion, thus being easier to implement in an experiment or a CFD code.

The model was suspended from downstream using a C-shaped bracket with a center mount for the balance and model. The bracket was mounted vertically in the test section of the tunnel, so that the center of rotation was a vertical axis through the center of the tunnel. Two separate synchronized servo motors on the top and bottom of the tunnel drove the pitching motion through a timing belt/arc sector 20:1 gear ratio setup.

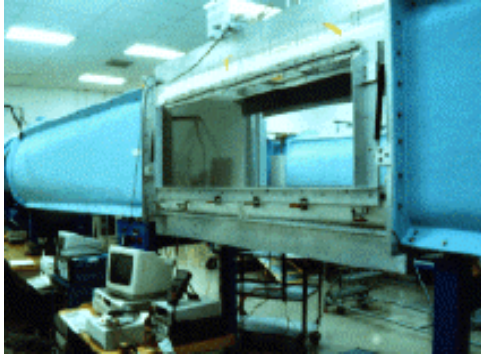


**Figure 4. USAF Academy 3 ft × 3 ft Lowspeed Wind Tunnel.**

The configuration was first tested in a static mode for angles of attack ranging from  $0^\circ \leq \alpha \leq 70^\circ$ ; lift and drag forces are presented in Fig. 5. As can be seen, the configuration has linear lift characteristics up to an angle of attack of about  $\alpha = 10^\circ - 12^\circ$ , with stall occurring at approximately  $\alpha = 20^\circ$ . The stall is not deep, however, and the configuration quickly re-establishes increasing lift up to  $\alpha = 32^\circ$ , where an abrupt loss of lift takes place. The cause of the increased lift above the stall angle of attack, and the loss of lift above  $\alpha = 32^\circ$  are assumed to be from the creation of leading-edge vortices that eventually breakdown or dissipate. The numerical simulation will be used to determine the exact cause of these results, including comments on how the configuration could be improved to further take advantage of vortex lift.

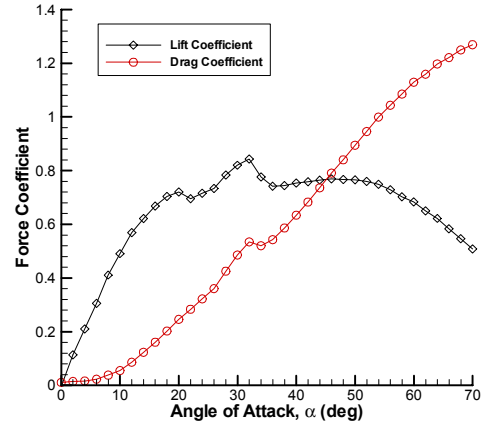


**Figure 5. Experimental Static Forces on UCAV 1301 Configuration.**

The configuration was then pitched at 0.5, 1.0, and 2.0 Hz ( $k=0.01$ , 0.02, and 0.04, respectively), with the center of rotation being at the nose, 35% MAC, and the tail. The pitch cycles were completed for three ranges of angle of attack,  $0^\circ \leq \alpha \leq 20^\circ$ ,  $16^\circ \leq \alpha \leq 35^\circ$ , and  $25^\circ \leq \alpha \leq 45^\circ$ . A representative set of experimental data is presented in Fig. 6, where the pitch rate is 2 Hz ( $k=0.04$ ) and the pitching is about the 35% MAC location (a nominal c.g. location). The static lift and drag results are also presented for reference.

Notice the hysteresis for  $0^\circ \leq \alpha \leq 20^\circ$ , with increased lift (relative to the static case) being obtained during the pitch-up motion through the past-stall region. During the pitch-down motion there is decreased lift for the remainder of the cycle. In addition, the hysteresis effect decreases as the angle of attack range increases. Also, while the pitching effect on lift is obvious, there is very little impact on the drag of the configuration. The results are quantitatively similar to airfoil results shown in Ref. 9, although airfoils rarely gain or lose lift at angles of attack in the linear range during the pitch-up motion. While these results are interesting and encouraging, very little knowledge was gained about the fluid dynamic processes that are involved in creating the experimental results.

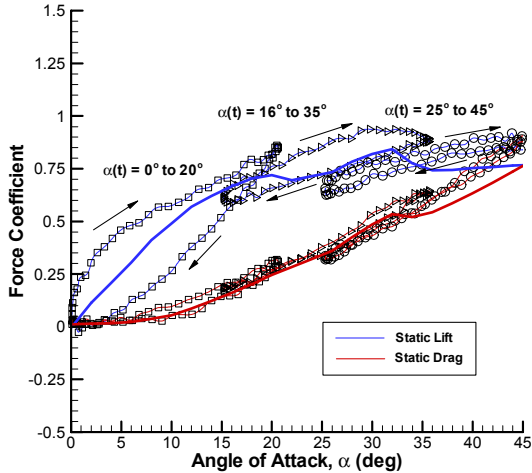


**Figure 6. Experimental Pitch-Up Forces (pitching about 35% MAC at 2 Hz,  $k=0.04$ ).**

Other representative results for pitching about the nose and tail are presented in Figs. 7 and 8, respectively. Figures 6-8 all use the same scales for comparison purposes. While these pitching centers are not feasible for conventional configurations, they could be attained with vectored thrust or pneumatic flow control. Notice that each of these cases has somewhat different characteristics than the 35% MAC case, with pitching about the tail providing the biggest differences when compared with the other cases.

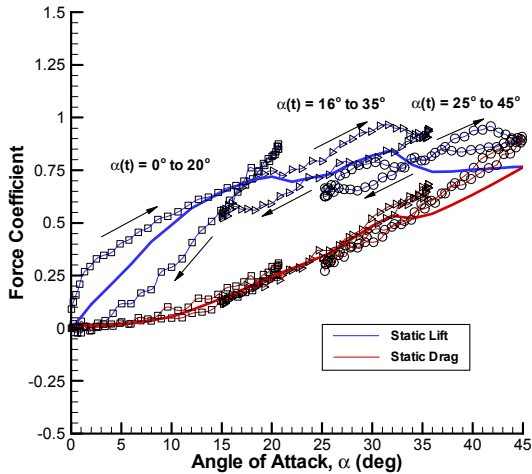


**Figure 7. Experimental Pitch-Up Forces (pitching about the nose at 2 Hz,  $k=0.04$ ).**

While the results for pitching about the nose (Fig. 7) only show slight differences when compared with the 35% MAC center of pitch results, pitching about the tail (Fig. 8) shows markedly different results. While the pitch-up portion of the cycle yields dramatically higher

lift coefficients in the post-stall region, the pitch-down lift is dramatically lower than the static results for most of the cycle. Pitching about the tail, while interesting, may not afford the overall increases in lift that would be of interest in a UCAV, with the lift increase during the pitch up being counterbalanced by the lift decrease during the pitch down, except in the post-stall region. This might lead to the use of various flow control methods to obtain similar results without the adverse impact on lift at the lower angles of attack.

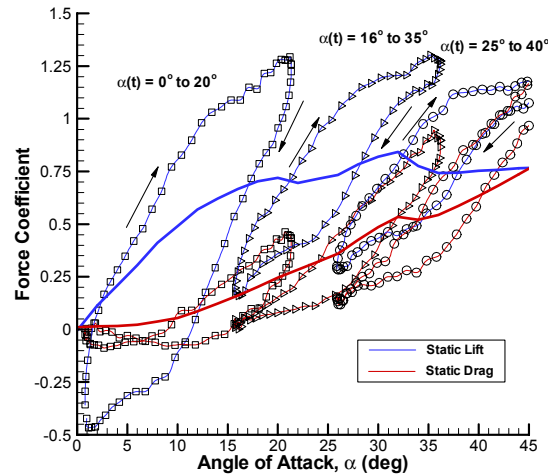


**Figure 8. Experimental Pitch-Up Forces (pitching about the tail at 2 Hz,  $k=0.04$ ).**

### Computational Results

The unstructured flow solver Cobalt was chosen because of its speed and accuracy; Cobalt is a commercial version of Cobalt<sub>60</sub>. Cobalt solves the Euler or Navier-Stokes equations, including an improved spatial operator and improved temporal integration. The code has been validated on a number of problems utilizing turbulence models, including the Spalart-Allmaras model (which forms the core of the DES hybrid turbulence model).<sup>15</sup> Tomaro, et al., converted Cobalt<sub>60</sub> from explicit to implicit, enabling CFL numbers as high as one million.<sup>16</sup> Grismer, et al., then parallelized the code, yielding a linear speedup on as many as 1024 processors.<sup>17</sup> Forsythe, et al., provided a comprehensive testing and validation of the RANS models, including the Spalart-Allmaras, Wilcox  $k-\omega$ , and Menter's turbulence models.<sup>18</sup>

The computations were performed on an Origin 2000 computer (using 30 processors) and a Beowulf cluster (using 38 processors). The

solutions were obtained using unstructured grids with a combination of prism and tetrahedrons. The meshes were generated for half of the configuration, with symmetry assumed about the configuration centerline in the spanwise direction. The centerline plane was modeled as a symmetry plane, the UCAV surface was modeled as a solid wall with a no slip condition, and the outer boundaries were modeled with freestream conditions. In order to more closely match the wind tunnel model, the inlet and exhaust areas of the configuration were covered over with solid surfaces. The outer boundary was placed 8 mean aerodynamic chords in front of, 10 mean aerodynamic chords behind, and 4.5 mean aerodynamic chords above and below the configuration.

The flowfield for the 1301 UCAV configuration was computed for three grids of varying sizes: 1.3 million, 2 million, and 4 million cells. The 2 million cell mesh is shown in Fig. 9. Mesh refinement was made in the region above the wing in order to more effectively model the leading-edge vortices and vortex breakdown above the wing.

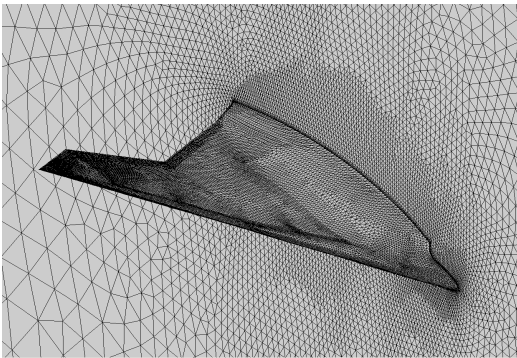


Figure 9. UCAV 1301 with 2 Million Cell Mesh.

A grid resolution study was performed with the three grids by running each grid to a steady-state solution at  $\alpha = 20^\circ$ . The normal force variation with iterations is shown in Fig. 10 for the coarse and medium grids, 1.3 and 2.0 million cells, respectively. While both solutions show that the results are somewhat unsteady, they have converged to the same normal force levels. Based on these results, all further computations have been performed on the 2.0 million cell mesh.

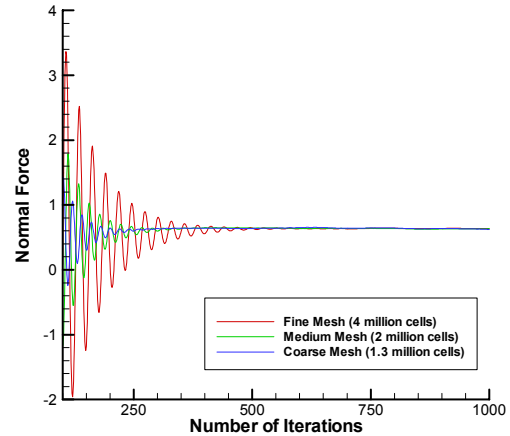


Figure 10. Grid resolution study at  $\alpha = 20^\circ$ .

Figure 11 shows a representative numerical simulation of the configuration at  $\alpha = 20^\circ$ , with the flowfield being visualized with streamlines and crossflow planes of  $x$ -vorticity. The leading-edge vortices are clearly visible closely following the  $50^\circ$  sweep, until approximately  $x/l = 0.40$  when vortex breakdown is evident. Low surface pressures are visible beneath the vortex prior to breakdown; these low pressures account for the lift on the configuration at  $\alpha = 20^\circ$ . After breakdown, the vortex wake quickly moves up and behind the leading-edge, leading to higher pressures on the upper surface of the wing. The vortices are very wide compared with their height, most likely due to the rounded leading edges of the wing. Secondary vortices are also visible beneath the primary vortices. The primary vortex is seen splitting into two vertical flow structures after the breakdown location.

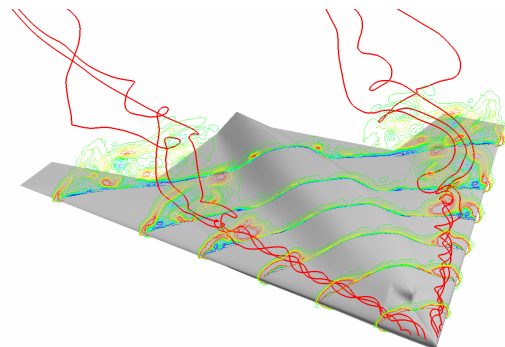
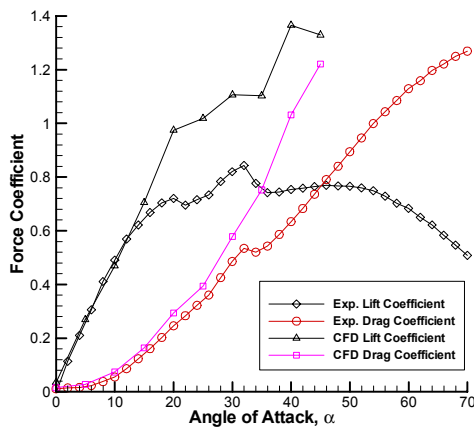


Figure 11. Steady Laminar Numerical Simulation (crossflow planes of  $x$ -vorticity with streamlines);

$$\alpha = 20^\circ, Re_{\bar{c}} = 1.42 \times 10^5.$$

Figure 12 shows a comparison between steady numerical results (first-order accurate in time) and the static experimental data. The results are quite good for the linear range of angle of attack, but do not capture the stall angle of attack, with the numerical prediction showing the flow remaining attached to a much higher angle of attack. Ordinarily, a fully laminar flow should separate sooner than a turbulent flow, so these results are most likely due to something other than transitional wind tunnel data, such as unsteadiness. The post-stall region is also not predicted well, although general trends seem to mimic the experimental data. Both the magnitudes for lift and drag coefficients are significantly in error when compared with the data.



**Figure 12. Numerical (Steady) and Experimental (Static) Force Coefficient Comparison.**

At  $\alpha = 25^\circ$ , the vortex breakdown location has moved forward significantly, with breakdown taking place at approximately  $x/l = 0.24$ . The low pressure region near the nose of the vehicle has become more pronounced, while the pressures over the aft portion of the configuration have increased when compared with the  $\alpha = 20^\circ$  case.

The numerical predictions for  $15^\circ \leq \alpha \leq 45^\circ$  were recomputed in time-accurate mode (second-order accurate in time with two Newton subiterations per time step,  $\Delta t = 0.00005 s$ ,  $\Delta t^* = 0.0075$ ). The post-stall results were fairly dramatically changed after the time-accurate runs (some of which took a considerable amount of time to reach a final solution), with much improved comparisons

between the predictions and the experimental data (see Fig. 13). While the stall region was still not modeled precisely, the computations show reasonable comparisons for most of the angle of attack range.

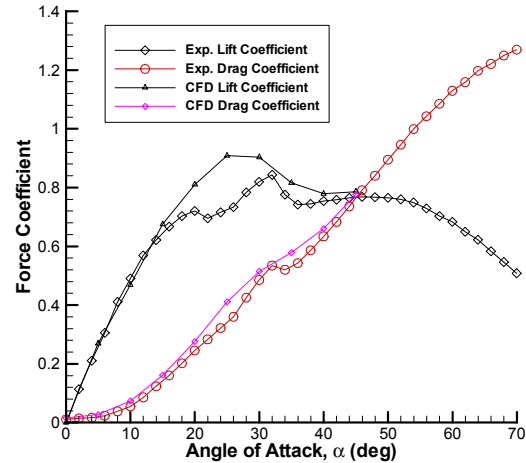


**Figure 13. Numerical (Time Accurate) and Experimental (Static) Force Coefficient Comparison.**

One of the purposes of the numerical simulation is to visualize the flowfield around the UCAV configuration at various angles of attack and determine what is causing the results seen in Fig. 13. A series of upper surface flowfield visualizations have been made at various angles of attack and are presented in Figs. 14a-14h; all figures use the same pressure scales for comparative purposes. At the lower angles of attack, such as  $\alpha = 5^\circ$  (Fig. 14a), the flow is fairly conventional, with streamlines flowing over the airfoil sections creating slightly lower pressures on the upper surface. A small region of separated flow is seen near the aft end of the configuration, however.

When the angle of attack is increased to  $\alpha = 10^\circ$  (Fig. 14b), most of the flowfield remains approximately the same, however a small vortex has developed along the leading-edge of the configuration. By the time  $\alpha = 15^\circ$  is reached (Fig. 14c), the leading-edge vortex is quite pronounced, although the vortex is already breaking down approximately half way along the leading edge. While this leading-edge vortex provides additional lift (note the decreased upper surface pressures), the additional lift is not enough to maintain a linear lift curve (see Fig. 13).

At  $\alpha = 20^\circ$  the leading-edge vortex breakdown location has moved forward noticeably, although the vertical flowfield is still maintaining low pressures on the upper surface. As the angle of attack is further increased to  $\alpha = 25^\circ$ , the leading-edge vortex is only impacting the forward section of the vehicle, but still producing considerable amounts of lift—the vortex can also be seen to have shifted toward the vehicle centerline, most likely due to the rounded leading edges on the vehicle. Rounded leading edges do not produce nearly as strong a vortex as sharp leading edges, and that impact is

certainly affected the lift of the configuration at these angles of attack.

Finally, by the time the vehicle reaches  $\alpha = 30^\circ$  and above, the burst vortex slowly gives way to a stalled upper surface, although the leading-edge is still producing a vortex that is creating lift near the front of the vehicle. This explains the fairly constant lift variation with angle of attack from  $32^\circ \leq \alpha \leq 50^\circ$  (see Fig. 13 and compare with Figs. 14f-14h).

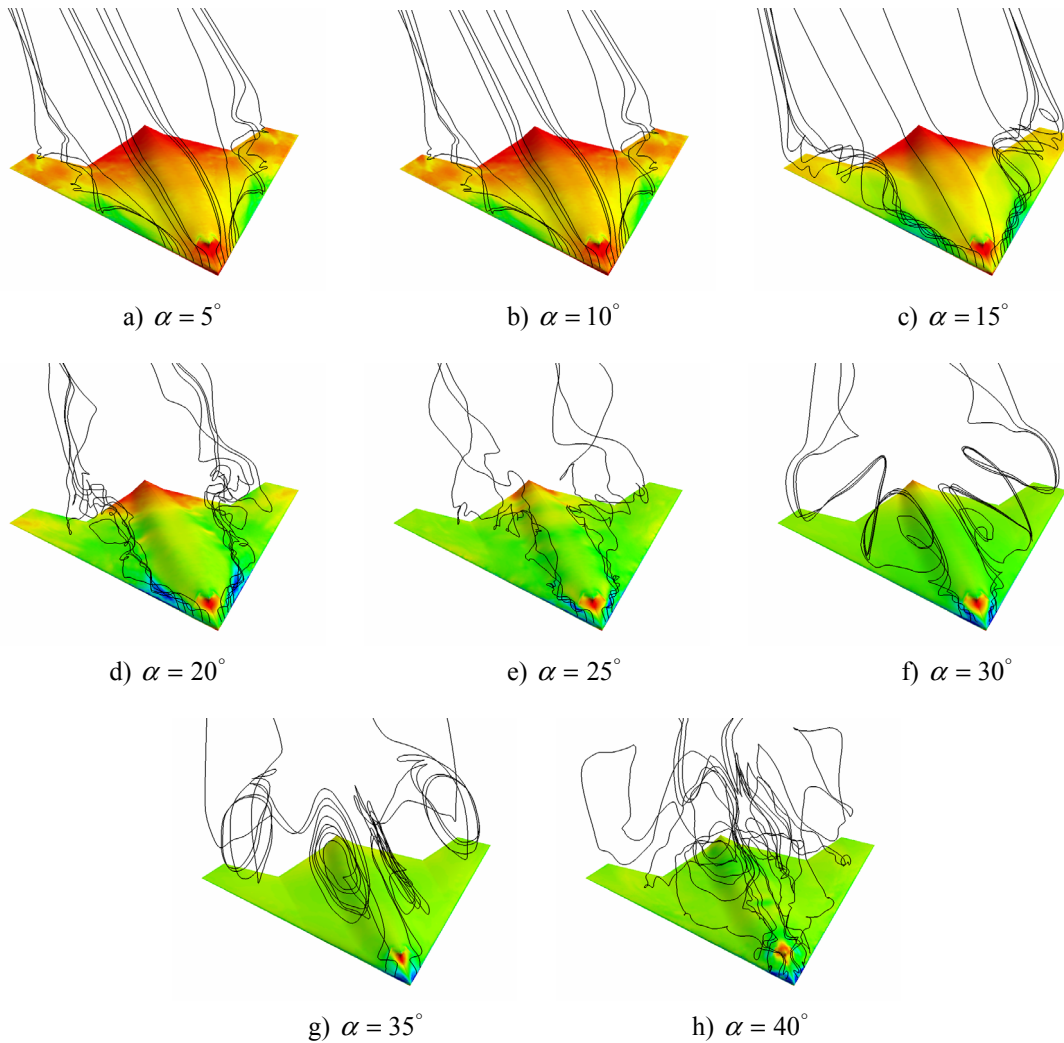


**Figure 14. Upper Surface Flowfields (surfaces colored by pressure).**

The 1301 UCAV configuration was then run in a dynamic pitchup to match the pitching motion of the wind tunnel test (see the pitchup equation previously defined). The case was run for the 2 Hz pitching motion with

pitching taking place about the 35% MAC location. The computations were run at a time step of  $\Delta t = 0.00005$  s, or a non-dimensional time step of  $\Delta t^* = 0.0075$ . The pitching was

initiated from  $\alpha = 0^\circ$  after running for 500 iterations and achieving a steady solution.

Fig. 15 shows the pitching results from the computational simulation compared with the wind tunnel data. The pitching cycle begins by transitioning from a steady flowfield and then approaches the pitch-up results from the wind tunnel test. The computations were run at a time step of  $\Delta t = 0.00005 s$ , with five Newton subiterations. One issue in the results is why the pitching characteristics are different from typical airfoil dynamic stall results, which normally pitch up along or near the static lift curve and then extend into the post-stall region (see Fig. 1). After reaching the maximum pitch angle, the lift usually drops below the static value for the remainder of the cycle. In the case of the 1301 UCAV, however, the lift is greater than the static case during the pitch up.

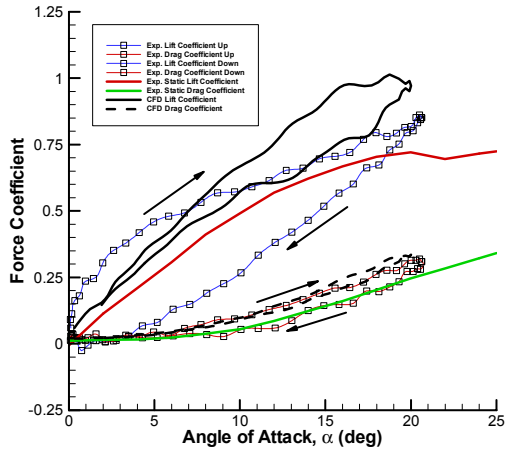


**Figure 15. Pitching Cycle Comparison; 2 Hz pitching about 35% MAC.**

Figures 16 through 18 help explain the results seen in Fig. 15. Figure 16 shows the UCAV upper surface pressure distribution for the time-accurate static case at  $\alpha = 15^\circ$ . Figures 17 and 18 present the same views for  $\alpha = 15^\circ$  from the pitch up and pitch down results, respectively. Notice that the leading-edge vortex for the pitch-up case is stronger (resulting in lower pressures), than the static result. This is the cause of the increase in lift during the pitch up: the dynamic motion creates a leading-edge vortex that is stronger than for the static case. While the aft portions of the upper surface seem to have slightly different pressures as well, it is believed that most of the dynamic lift is coming from the leading-edge vortex. Since the pitch-up vortex is stronger, vortex

breakdown could also take place at lower angles of attack, so there is a trade-off between increased lift during pitch-up and loss of the lift as the vortex breakdown location moves forward on the vehicle. This may explain the change in the incremental lift produced while pitching up (see Fig. 15 where the difference between the pitch-up lift and the static lift is different at lower angles of attack than at higher angles of attack).

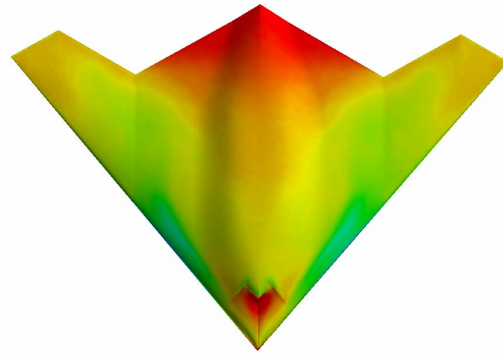


**Figure 16. Static Pressure Distribution,  $\alpha = 15^\circ$ .**

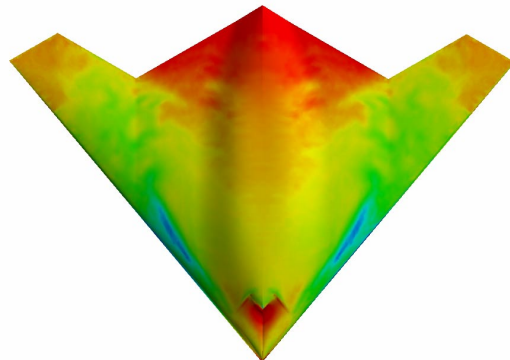


**Figure 17. Pitch-Up Pressure Distribution,  $\alpha = 15^\circ$ ; 2 Hz pitching about 35% MAC.**

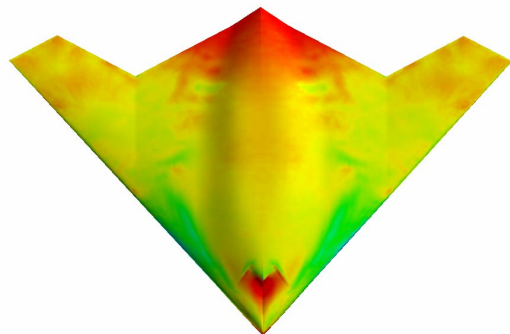


**Figure 18. Pitch-Down Pressure Distribution,  $\alpha = 15^\circ$ ; 2 Hz pitching about 35% MAC.**

## Conclusions

A representative unmanned combat aerial vehicle (UCAV) has been studied computationally and experimentally. The Boeing 1301 UCAV configuration, similar in shape to the X-45A, is a candidate configuration for future UCAV applications, where increased maneuverability and flight capabilities will be important. In order to assess the capabilities of such a configuration, the high angle of attack and pitching characteristics of the vehicle have been assessed.

While the 1301 UCAV is not, in general, an optimum aerodynamic configuration, it does have interesting aerodynamic characteristics. For example, in spite of the use of a rounded leading edge, a leading-edge vortex is clearly developing at  $\alpha = 10^\circ$ , and the vortex enables the configuration to continue developing lift up to  $\alpha = 25^\circ$ . In the post stall region, the vehicle continues to maintain lift, in spite of the fact that the leading-edge vortex has clearly broken down.

The pitching characteristics of the vehicle are somewhat unusual when compared with pitching airfoils and simpler wing geometries. Instead of gaining lift during a pitch-up maneuver (when compared with the static lift characteristics), the 1301 UCAV actually loses lift until the post stall region is reached. During the pitch down maneuver, the aircraft gains lift compared to the static case.

## Acknowledgments

The authors wish to thank James R. Forsythe for his help with using the Cobalt flow solver. We also thank Boeing Military Aircraft in St. Louis, MO for providing the UCAV 1301 geometry.

## References

1. Gern, F.H., Inman, D.J., and Kapania, R.K., "Computation of Actuation Power Requirements for Smart Wings with Morphing Airfoils," AIAA Paper 2002-1629, Apr. 2002.
2. Gern, F.H., Inman, D.J., and Kapania, R.K., Structural and Aeroelastic Modeling of General Planform UCAV Wings with Morphing Airfoils," AIAA Paper 2001-1369, Apr. 2001.
3. "Boeing to Develop UAVs with Advanced Propulsion," *Fuel Cells Bulletin*, Nov. 2002, pp. 4-5.
4. Huang, A., Folk, C., Silva, C., Christensen, B., Chen, Y., Ho, C.M., Jiang, F., Grosjean, C., Tai, Y.C., Lee, G.B., Chen, M., and Newbern, S., "Application of MEMS Devices to Delta Wing Aircraft: From Concept Development to Transonic Flight Test," AIAA Paper 2001-0124, Jan. 2001.
5. Capozzi, B.J. and Vagners, J., "Evolving (Semi)-Autonomous Vehicles," AIAA Paper 2001-4241, Aug. 2001.
6. Guilmineau, E. and Queutey, P., "Numerical Study of Dynamic Stall on Several Airfoil Sections," *AIAA Journal*, Vol. 37, No. 1, 1999, pp. 128-130.
7. Greenblatt, D., Neuberger, D., and Wagners, J., "Dynamic Stall Control by Intermittent Periodic Excitation," *Journal of Aircraft*, Vol. 38, No. 1, 2001, pp. 188-190.
8. Carr, L.W., Chandrasekhara, M.S., and Wilder, M.C., "Effect of Compressibility on Suppression of Dynamic Stall Using a Slotted Airfoil," *Journal of Aircraft*, Vol. 38, No. 2, 2001, pp. 296-309.
9. Ekaterinaris, J.A. and Platzer, M.F., "Computational Prediction of Airfoil Dynamic Stall," *Progress in the Aerospace Sciences*, Vol. 33, 1997, pp. 759-846.
10. Carr, L.W., "Progress in Analysis and Prediction of Dynamic Stall," *Journal of Aircraft*, Vol. 25, No. 1, 1988, pp. 6-17.
11. Henkner, J., "Phenomena of Dynamic Stall on Swept Wings," 22<sup>nd</sup> International Congress of the Aeronautical Sciences, ICAS Paper 2000-2.9.2, Aug.-Sep. 2000.

12. Coton, F.N. and Galbraith, R.A., "An Experimental Study of Dynamic Stall on a Finite Wing," *Aeronautical Journal*, Vol. 103, May 1999, pp. 229-236.
13. Morgan, P.E. and Visbal, M.R., "Simulation of Unsteady Three-Dimensional Separation on a Pitching Wing," AIAA Paper 2001-2709, June 2001.
14. Schatz, M., Bunge, U., and Rung, T., "Computational Modeling of Pitching Airfoil Flows," <http://hodgson.pi.tu-berlin.de/~schatz/PIZIALI/osc.html>.
15. Strang, W. Z., Tomaro, R. F., Grismer, M. J., "The Defining Methods of Cobalt<sub>60</sub>: A Parallel, Implicit, Unstructured Euler/Navier-Stokes Flow Solver," AIAA Paper 99-0786 Jan. 1999.
16. Tomaro, R.F., Strang, W. Z., and Sankar, L. N., "An Implicit Algorithm for Solving Time Dependent Flows on Unstructured Grids," AIAA Paper 97-0333, Jan. 1997.
17. Grismer, M. J., Strang, W. Z., Tomaro, R. F. and Witzemman, F. C., "Cobalt: A Parallel, Implicit, Unstructured Euler/Navier-Stokes Solver," *Advances in Engineering Software*, Vol. 29, No. 3-6, 1998, pp. 365-373.
18. Forsythe, J.R., Strang, W., Hoffmann, K.A., "Validation of Several Reynolds-Averaged Turbulence Models in a 3D Unstructured Grid Code," AIAA Paper 2000-2552, June 2000.